

High current limits in chemical vapor deposited graphene spintronic devices

Daria Belotcerkovtceva^{1,§}, J. Panda^{1,§}, M. Ramu², Tapati Sarkar², Ulrich Noumbe¹, and M. Venkata Kamalakar¹ (✉)

¹ Department of Physics and Astronomy, Uppsala University, Box 516, Uppsala SE-751 20, Sweden

² Department of Materials Science and Engineering, Uppsala University, Box 35, Uppsala SE-751 03, Sweden

§ Daria Belotcerkovtceva and J. Panda contributed equally to this work.

© The Author(s) 2022

Received: 29 May 2022 / Revised: 20 September 2022 / Accepted: 7 October 2022

ABSTRACT

Understanding the stability and current-carrying capacity of graphene spintronic devices is key to their applications in graphene channel-based spin current sensors, spin-torque oscillators, and potential spin-integrated circuits. However, despite the demonstrated high current densities in exfoliated graphene, the current-carrying capacity of large-scale chemical vapor deposited (CVD) graphene is not established. Particularly, the grainy nature of chemical vapor deposited graphene and the presence of a tunnel barrier in CVD graphene spin devices pose questions about the stability of high current electrical spin injection. In this work, we observe that despite structural imperfections, CVD graphene sustains remarkably highest currents of 5.2×10^8 A/cm², up to two orders higher than previously reported values in multilayer CVD graphene, with the capacity primarily dependent upon the sheet resistance of graphene. Furthermore, we notice a reversible regime, up to which CVD graphene can be operated without degradation with operating currents as high as 10^8 A/cm², significantly high and durable over long time of operation with spin valve signals observed up to such high current densities. At the same time, the tunnel barrier resistance can be modified by the application of high currents. Our results demonstrate the robustness of large-scale CVD graphene and bring fresh insights for engineering and harnessing pure spin currents for innovative device applications.

KEYWORDS

chemical vapor deposited (CVD) graphene, high current density, graphene spintronics, spin integrated circuits, graphene spin valve

1 Introduction

Over the last decade, the field of two-dimensional (2D) nanoelectronics and spintronics [1] has witnessed enormous advancements in using graphene for new applications that show promise for memory-logic integrated circuits, including neuromorphic components. In particular, attaining high performance in wafer-scale commercial systems is necessary for graphene spintronic sensors and circuits to take off. Yet, challenges remain when it comes to the feasibility of applications such as spin torque effects [2] and spin torque oscillators [3] that require high current carrying capacity and stability. Even nanodevices using copper have a current carrying limitation of $\sim 10^6$ A/cm². Today, the advancement of the chemical vapor deposition method has enabled the production of practical and industry-compatible large-area graphene [3, 4]; with commercial graphene being readily available, it presents real prospects in high-quality charge and spin transport devices [5]. For example, competitive spin transport achieved in monolayer chemical vapor deposited (CVD) graphene [6, 7], including on flexible substrates [8], and recent reports of ultimate spin current capabilities using CVD graphene [9], even under ambient conditions, show massive scope for the growth of graphene spintronic applications. However, when it comes to current carrying capacity, the grainy structure of CVD graphene and tunnel barriers utilized in

spintronic devices pose a question on the limitation of the maximum current applicable in such devices. Past studies, mainly performed on mechanically exfoliated few-layer graphene nanoribbons obtained from Kish graphite, have shown a breakdown current density of $\sim 10^8$ A/cm² [10, 11], including results obtained in bilayer graphene [12]. Compared to these reports on exfoliated systems, current stress investigation on multilayer CVD graphene revealed one order less maximum breakdown current density $\sim 4 \times 10^7$ A/cm² [13]. Recently, a current density of 1.18×10^8 A/cm² was reported in 300 nm channels of CVD graphene contacted by metal electrodes [14]. Since the size of the graphene channel is too small here to contain grain boundaries or ripples, such a value matches well with measurements on single crystalline exfoliated graphene flakes. However, considering this size is less than the typical micron range crystal size in CVD graphene, the current carrying capacity of large-scale CVD graphene is still unclear. Especially, earlier results in polycrystalline samples showed one order lower current density [13]. While CVD graphene presents significant scope for scalability and practical applications, it exhibits intrinsic defects, grain boundaries, wrinkles, and transfer/fabrication-accrued impurities, that are known to limit the electrical performance of these devices. CVD graphene grown over Cu substrate is reported to feature grain sizes of a few microns [15]. Commercial graphene

Address correspondence to venkata.mutta@physics.uu.se

displays typical grain boundaries/ripples in the size range of 2–5 μm , confirmed through multiple techniques [16] (displayed later in Fig. 1). The nanoscale defects of grain boundaries and wrinkles increase electrical resistance, and consequently can act as hot spots where localized resistive heating and breakdown can occur preferentially [17]. Localized Joule heating in grain boundaries tends to constrict device shape leading to further defect formations. For devices longer than 5 μm , local high-temperature spots can arise due to grain boundaries and wrinkles, subsequently affecting current limits of the spin devices. On a smaller scale, heated grain boundaries cause heat flow leading to faster device failure. Therefore, understanding the stability and maximum current carrying capacity of CVD graphene spin channels and contacts under the influence of high current is crucial for developing high spin current generation capabilities and spin current interconnect applications for spin integrated circuits.

In this work, we demonstrate a very high current carrying capacity in monolayer CVD graphene with a breakdown current density of sub- 10^9 A/cm^2 . Through elaborate 2-probe and 4-probe measurements, we uncover a distinct channel behavior upon high current stress and range up to which CVD graphene channel can be electrically operated and how breakdown current density varies with graphene sheet resistance. We also explore spin transport in such channels with high electrical currents of 1 mA ($\sim 10^8 \text{ A/cm}^2$), stability of several hours of long-term current passage, and the response of contacts to such high currents.

2 Results and discussion

To investigate the current carrying capacity of monolayer CVD graphene-based spin devices, we fabricated graphene spin devices using commercial CVD graphene on Cu (Graphenea, Spain), with multiple TiO_x/Co electrodes for spin injection and detection. Raman spectrum indicating the monolayer nature of CVD graphene is shown in Fig. S1 in the Electronic Supplementary Material (ESM). We also performed atomic force microscopy (AFM) of our CVD graphene on Si/SiO_2 substrate as well as of the patterned device structures, which reveals grains and wrinkles in the μm range, as shown in Figs. 1(a) and 1(b). The detailed device fabrication procedure is explained in the Methods section. Figure 1(c) shows a schematic of a patterned CVD graphene with ferromagnetic tunnel contacts. To determine the electrical

properties of graphene and contact interfaces, we first performed low current electrical transport measurements in several configurations. Four probe gate dependence measurements yielded field-effect electron mobility $\sim 1,750 \text{ cm}^2/(\text{V}\cdot\text{s})$ (Fig. 1(d)), which demonstrates that our devices show reasonable mobility needed to establish good quality spin transport. A high n-type doping was intrinsic to the as-prepared devices and can be primarily attributed to the interaction with the substrate and dangling bonds that are expected in the top 280 nm SiO_2 layer of the Si/SiO_2 substrate, which can promote charge transfer across the graphene- SiO_2 interface. Other causes that contribute to the n-type doping are fabrication process steps that involve solvents, reactive ion etching for patterning graphene, and electrode realization [9, 18]. Low current characterization of channel, contacts, and spin valve signal are shown in Fig. S2 in the ESM. Following these initial measurements, we performed high-current stressing experiments, first with two terminals (2T), a standard method employed in past studies. As shown in Fig. 1(e) (I - V characteristics), the current (I) increases with an applied bias voltage (V), and at a specific high current, the graphene breakdown occurs, resulting in an abrupt drop in the current. The non-linear 2T I - V curve at low voltages confirms tunneling behavior across the oxide tunnel barrier interfaces with graphene (Fig. 1(e)). However, a continuous reduction in slope at higher currents can be attributed to a heating-related cumulative increase in the graphene channel resistance. To further determine the actual response of graphene channels, we performed four-terminal (4T) I - V measurements (Fig. 1(f)), which revealed linear I - V characteristics up to a high current of 2 mA ($\sim 10^8 \text{ A/cm}^2$) with graphene sheet resistance $\sim 0.5\text{--}2 \text{ k}\Omega/\square$. Interestingly, a sharp onset of non-linear saturation behavior was also observed. While this can be attributed to the increase in resistance due to Joule heating and cumulative effects, the overall behavior depends upon the competition between the rate of heating in graphene and the rate of heat dissipation in the SiO_2/Si substrate.

As seen in the repeated cyclic measurements performed in the four-terminals scheme (4T) (Fig. 1(f)), the channel resistance undergoes changes beyond a specific current density. Since these devices are broken after each high current measurement, we presented our overall observations on several devices showing different sheet resistances. The current saturation regime divides the I - V curve into reversible and non-reversible, where self-

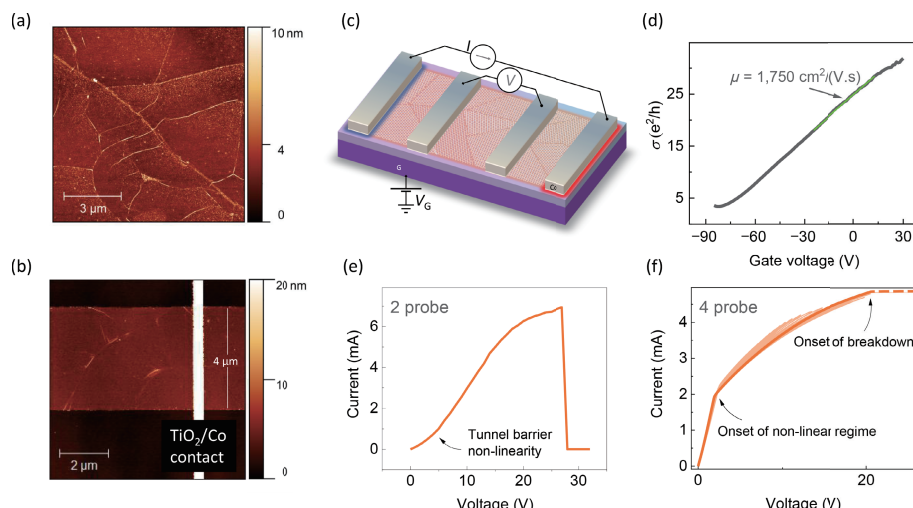


Figure 1 AFM image of (a) graphene over 10 $\mu\text{m} \times 10 \mu\text{m}$ area with distinguished wrinkles and ripples, and (b) graphene channel near contact region of a device with corresponding actual width. (c) Schematic of a graphene device in four-probe measurement technique. (d) Gate dependence with extracted mobility at low bias currents. (e) 2-terminal I - V curve of the CVD graphene undergoing electrical breakdown. (f) 4-terminal I - V characteristics with constantly increasing sweep range. The onset of breakdown is typical of the current source response as the voltage measured by the voltmeter abruptly reaches the compliance voltage limit of the current source.



heating can be observed at a high current (Fig. 2(a)). To examine the transition between the two regimes, I - V curves were recorded within cycles with the varying maximum current in steps ($I_{\text{step}} = 0.2 \text{ mA}$, between 0–3 mA). Despite the high current carrying capacity, the CVD graphene channel degradation due to cumulative Joule heating can lead to an irreversible regime. The transition between reversible and irreversible regimes is observed to occur at a specific value of current ($I_{\max \text{ rev}}$) in each cycle, and the sheet resistance of the graphene channel changes after each cycle beyond the reversible regime. The behavior of $I_{\max \text{ rev}}$ for each cycle is found to characteristically vary with the sheet resistance, as displayed in the inset of Fig. 2(a), as a higher resistance requires a lower maximum current to modify the graphene sheet. However, keeping the operation of the device in the current range less than $I_{\max \text{ rev}}$ ($\sim 10^8 \text{ A/cm}^2$) allows graphene not to overheat and endure stable sheet resistance, as shown in Fig. 2(b). This implies that graphene devices on Si/SiO₂ can be operated with heat dissipation managed by the substrate Si/SiO₂ efficiently within the $I_{\max \text{ rev}}$ limit. Such information is particularly crucial because, while high current carrying capacity is known in graphene, the degradation has never been explicitly understood. The present study involving 4T measurement allows us to enlighten this issue for the first time. Furthermore, this allows us to isolate the role of contacts and only unveil the impact of high current stressing on graphene channels.

To fully determine the current-carrying capacity of the CVD graphene spin devices, including the tunnel contacts, we have measured the I - V characteristics of different graphene devices with varying sheet resistances extending up to 20 k Ω and above. A typical high field I - V characteristic is shown in Fig. 1(e) with increasing bias voltage until the graphene breakdown occurs at higher currents of several mA. Figure 2(c) shows the current density measured as a function of the CVD graphene sheet resistance for breakdown and reversible regimes for low sheet resistance devices (< 3 k Ω). The breakdown current density (J_b) values for these spin devices were in the range of $2\text{--}5.2 \times 10^8 \text{ A/cm}^2$. The values of J_b observed in our monolayer CVD graphene spin devices are comparable to the breakdown current densities seen in the previously reported bilayer/multilayer graphene and

graphene nanoribbons [11, 13, 19]. Also, as shown in Fig. 2(c), the reversible current density (at the onset of saturation) of these devices was found to be $\sim 10^8 \text{ A/cm}^2$, which suggests that our spin devices can be operated at high currents, beyond the typical current densities needed for spin-transfer torque applications. For most of our devices, the sheet resistance was found to have a typical value < 8 k Ω , with some devices closer to 20 k Ω and higher. To uncover the qualitative behavior of the breakdown current density of the CVD graphene with sheet resistance, we measured J_b as a function of sheet resistance of several devices, including devices that displayed high sheet resistance. As shown in Fig. 2(d), CVD graphene channels with higher sheet resistance exhibit lower J_b values and are more likely to undergo breakdown for the same current density. Defects, wrinkles, grain boundaries, and impurities increase the effective resistivity and result in high resistive sheets. The behavior in Fig. 2(d) can be understood from the fact that considering the same substrate heat dissipation and similar breakdown temperature for all CVD graphene sheets, higher resistance would require a lower current (assuming breakdown power density $J_b^2 \times R_{\square} \approx \text{const}$ for all our samples leads to $J_b \propto 1/\sqrt{R_{\square}}$) for channel breakage. Note that in these spin devices, the value of J_b also includes the tunnel barrier resistive contact region that could degrade at high current densities. Despite this, in the inset of Fig. 2(d), we show the fit of $J_b \propto R_{\square}^{-\alpha}$, and obtain $\alpha \approx 0.32$, which is reasonably close to the expected value of $\alpha = 0.5$. These results suggest that CVD graphene with sheet resistance lower than k Ω can have a high breakdown current density of $\sim 10^9 \text{ A/cm}^2$, which could be achieved by highly doped graphene by surface charge transfer doping without degrading the electrical quality of graphene [18] and using high thermal conductivity substrates for greater heat dissipation.

As displayed in Fig. 3(a), the CVD graphene channels show nonlocal (NL) spin transport at high currents. In the NL measurement scheme shown in the inset of Fig. 3(b), spin-polarized currents are electrically injected into the graphene channel through the current circuit (I), and the resulting diffusion of pure spin current at a distance of L is detected by the voltage circuit (V_{NL}). Such isolation of the current and voltage circuits

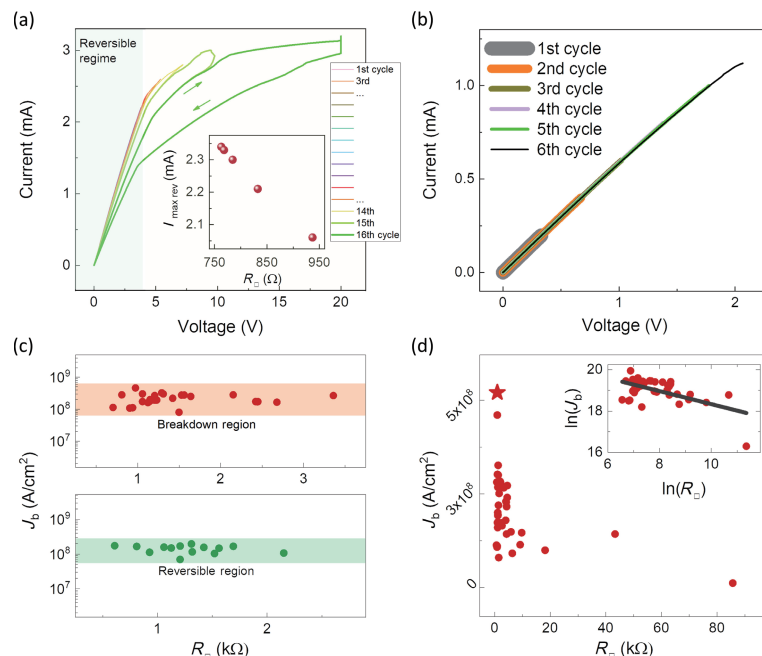


Figure 2 (a) Measured 4T I - V curve cycles with linear (reversible) and non-linear (non-reversible) regimes at high voltage ($V > 4.5 \text{ V}$). Inset: $I_{\max \text{ rev}}$ versus sheet resistance of graphene for each cycle beyond $I_{\max \text{ rev}}$. (b) 4T I - V curve cycles of the device within the reversible regime. (c) Measured maximum current density versus sheet resistance in different devices. (d) Breakdown current density as a function of sheet resistance of the CVD graphene (the star symbol indicates the maximum breakdown of current density obtained in our devices). Inset: current density versus sheet resistance fitted to $J_b \propto R_{\square}^{-\alpha}$.

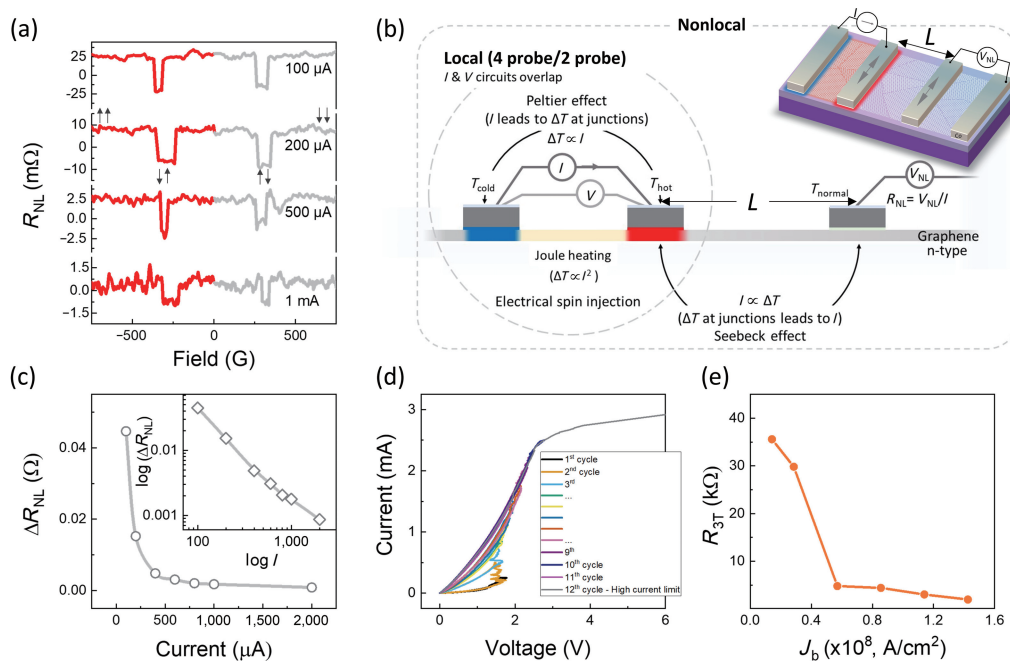


Figure 3 (a) Spin transport signal measured in the spin-valve geometry showing switching between parallel ($\uparrow\uparrow$ or $\downarrow\downarrow$) to antiparallel ($\downarrow\uparrow$ or $\uparrow\downarrow$) configurations of the injector and detector electrodes at different applied currents. (b) Local and nonlocal measurement configurations in graphene spin devices, with depiction of thermoelectric effects such as Joule heating, Peltier effect, and Seebeck effect in a device. (c) Nonlocal resistance as a function of applied current from spin-valve transport measurements. The inset shows the logarithmic dependence of the plot. (d) Consecutive multiple 3T I - V cycles with increasing maximum applied current and electrical breakdown in the 12th cycle. (e) Contact resistance (measured at 100 mV) versus maximum applied current density in a measurement cycle.

allows for reliable measurement of pure spin accumulation, eliminating spurious magneto-resistive contributions associated with direct charge currents. Further details of the spin transport measurements can be found in the ESM. As shown in Fig. 3(a), clear spin valve signals were observed at very high spin injection currents of 100 \$\mu\$A–1 mA, implying that even at current densities \$\sim 10^8\$ A/cm\$^2\$, graphene channels endure and show spin diffusion. Considering a large injector-detector separation of $L = 10$ \$\mu\$m, the observed spin signals are reasonable for standard spin polarization of Co|TiO₂ injectors into graphene and of similar order as previously reported on Si/SiO₂ devices [6, 20, 21]. Interestingly, the nonlocal resistance strongly depends on the applied current (Fig. 3(c)), with the spin signal amplitudes heavily quenched at very high currents of 1 mA (\$\sim 10^8\$ A/cm\$^2\$). In graphene devices carrying high currents (both 2-probe or 4-probe measurements, shown in Figs. 1 and 2, respectively), while Joule heating occurs in the current carrying graphene channel, Peltier heating/cooling can take place at junctions [17, 22] (illustrated in Fig. 3(b)), which can be revealed by thermography techniques [23, 24]. On the other hand, in the nonlocal measurement geometry employed in the spin transport measurement, the spin injection circuit only involves spin current, and the corresponding graphene strip undergoes Joule heating. In addition, in this part, heating/cooling is expected to occur at the interface between graphene and TiO₂|Co due to the Peltier effect [17, 22]. Since the width of the contacts in our devices (\$\sim 100\$ nm) is much smaller than the characteristic contact transfer length for the interface materials involved (\$\sim 1\$ \$\mu\$m), we can rule out the contribution of the current crowding effect [17]. In the pure spin diffusion channel (between injector and detector), with no direct electrical bias across the injector and detector, in principle no Joule heating is expected, although a temperature difference between the contacts could lead to some Seebeck voltage [25]. Because graphene exhibits slow electron-lattice cooling rates, the thermoelectric effects are likely to contribute to the baseline in V_{NL} [26]. In addition, due to the negligible temperature gradient across the graphene-tunnel barrier-ferromagnet injector interface (as electric current passes through

the whole stack at the contacts), any thermal spin voltage is expected to be negligible compared to actual electrically-created nonlocal spin voltage [27]. Therefore, the behavior of spin valve amplitude at high currents can be ascribed to hot electrons due to a high voltage drop (at high current) across the injector interface. Such high voltage bias can result in enhanced ferromagnet-tunnel barrier interface spin excitations, leading to higher electron-magnon spin-flip scattering, which is expected to quench spin polarization [28–30]. In addition, change in barrier profile, a higher channel resistance due to cumulative heating, and possible reduced contact resistance at higher bias/high temperature are further expected to contribute to the observation of lower spin valve signals at higher current [31]. The tunnel barrier response to high currents is not known here. In particular, considering the oxide nature of the barrier, contact resistance modulation is expected. To understand that, three terminals (3T) cyclic measurements up to high currents were performed. As shown in Fig. 3(d), the resistance of the barrier was seen to decrease at high injection currents. While some contacts showed high current sustainability and typical tunneling I - V characteristic curves till high currents (as shown in Fig. S3(a) in the ESM), high resistive contacts (due to high voltage drop across interfaces) showed a decrease in resistance upon high current stressing. Such a decrease at relatively high voltage could be ascribed to the possible formation of conducting nanofilaments in the Co|TiO₂|graphene junction due to naturally oxidized ultra-thin oxide, and consequent high current density and contact enhanced spin relaxation in graphene, which could contribute to the enhanced quenching of spin signal in Fig. 3(c). In Fig. 3(e), we show low bias (100 mV) contact|graphene interface resistance as a function of the high current. Interestingly, our experiments reveal here for the first time that the channel and contact resistances exhibit very different responses to high currents. While the channel resistance remains unchanged in a reversible/stable regime up to high current densities, the contact resistance changes due to the possible formation of filaments in the \$10^8\$ A/cm\$^2\$ current density regime. In our devices, the tunnel barrier (Gr/TiO_x/Co junction) is

expected to exhibit non-stoichiometric ultra-thin metal oxide. High electric field/high voltage bias across the ultrathin barrier (\sim nm) can facilitate Ti nanofilament formation or oxygen ion migration across the junction, which can explicate the 3T graphene|ferromagnetic tunnel contact resistance reduction when subjected to high current density.

Finally, to test the endurance of the contacts and channels in our spin devices, we have performed time-dependent measurements at current densities $\sim 10^8$ A/cm² in graphene spin devices. Figure 4(a) shows time-dependent 3T (contact resistance) and 4T (graphene resistance) measurements. While the resistance of the contacts changes at high currents, the channel resistance stays fairly stable for a long time at high currents. Note that, in comparison to the 3T cyclic measurements on contacts in Fig. 3(d), where high current reduces the contact resistance, due to the possible formation of conducting filaments across the interface, measurement at constant high current over longer periods could lead to breakage and reformation/increase in density of the nanofilaments under high current stress. This could explain the initial increase in resistance in Fig. 4(a) till the stabilization in resistance is attained by the reformation of nanofilaments with enhanced current carrying capacity. Since the graphene channel survives till high currents and electromigration [32], considering interface thermal and conductivity mismatch and lower current carrying capacity of metals, the high current density is expected to affect the metal contact pads before the breakdown of graphene. Figure 4(b) shows the optical images of the CVD graphene devices before and after the breakdown limit. The images reveal faster degradation of thick metal contacts than CVD graphene, despite the single-layer nature of graphene here. These experiments suggest that ultrathin tunnel barriers with higher resistance undergo modification in resistance. The tunable interface resistance with thicker tunnel barriers could have potential in synaptic spin-valve memristors. On the other hand, a possible way

to avoid oxygen-migrated filament formation in conventional oxides could be to employ stable amorphous carbon interfacial layers [33], hexagonal boron nitride [34–36], or fluorographene [37] due to their structural integrity. Furthermore, with the advent of atomically thin 2D magnets and their sinterfaces [38], the high-current electromigration issues with conventional ferromagnetic thin films could possibly be mitigated.

3 Conclusions

In summary, graphene spintronic devices were investigated to determine the ultimate current carrying capacity through monolayer CVD graphene and ferromagnetic tunnel contacts. We observed the highest current carrying capacity in monolayer CVD graphene, with a breakdown current density of 5.2×10^8 A/cm², an order higher than the previously reported values in multilayer CVD graphene interconnects. By systematic four-terminal and three-terminal measurements, for the first time, we uncovered a reversible regime $\sim 10^8$ A/cm² up to which the graphene on Si/SiO₂ substrate remains stable and exhibits long-term durability. In addition, with high electrical currents up to $\sim 10^8$ A/cm², we observed spin valve signal and tunnel barrier resistance modifications by possible conductive nanofilament formation at high currents. Our work offers insights on high current limits in graphene spintronics devices, a reversible regime up to which devices can be operated without degradation, possibilities for implementing barrier resistance modulation, and further engineering opportunities for efficient graphene spintronic applications.

4 Methods

4.1 Device fabrication

Graphene spin devices were fabricated using commercially obtained CVD graphene on Cu (Graphenea, Spain) transferred over a 4-inch Si wafer. The CVD graphene with $\sim 4\text{--}5$ μm width and ~ 60 μm long stripes was patterned using optical lithography followed by oxygen plasma etching with 50 W power. The remaining photoresist was then removed using hot acetone at 70 °C for 10 min, followed by isopropanol rinsing for 5 min. Next, ferromagnetic tunnel contacts with different widths were patterned on graphene stripes using electron beam lithography and metal lift-off. An optimized layer of 0.8 nm evaporated titanium metal for these electrodes was first oxidized to form a tunnel barrier layer of TiO_x. Following this, e-beam-assisted metal evaporation was performed to deposit successive layers of 60 nm Co and 5 nm Al. Finally, lift-off was achieved in hot acetone and rinsed by isopropyl alcohol (IPA). The obtained devices featured contacts with widths of 150–350 nm and an active contact area with graphene of ~ 1 μm^2 . The devices were imaged using an optical microscope, with the optical parameters adjusted to observe the contrast of graphene over SiO₂/Si.

4.2 Raman spectroscopy

The single-layer nature of CVD graphene was confirmed by Raman spectroscopy. Spectra were obtained in the range 1,000–3,200 cm⁻¹ under 532 nm laser excitation.

4.3 Spin transport and electrical measurements

Spin transport measurements in spin-valve and Hanle configurations were performed using Keithley current source and nano-voltmeter in high vacuum condition with a room temperature electromagnet set up. The magnetic field sweep was carried out in the range $-1,000$ to $1,000$ G. The electrical three-

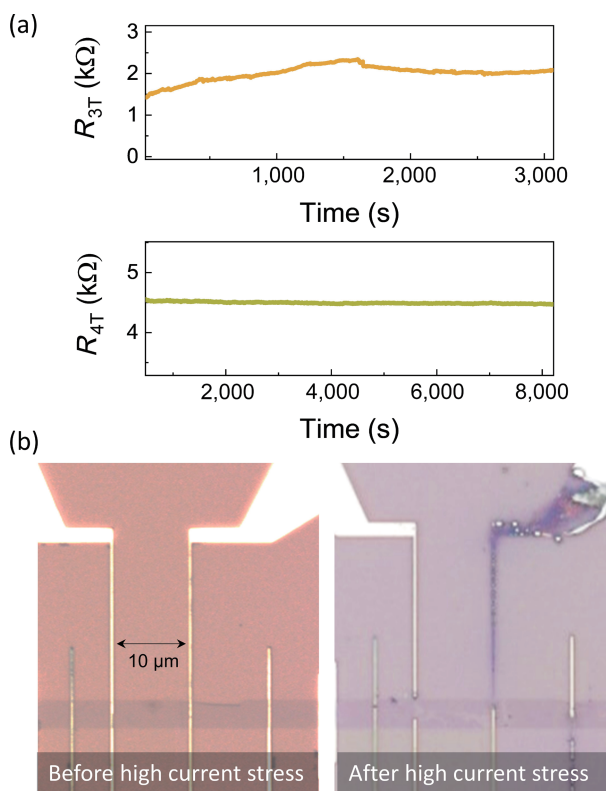


Figure 4 (a) Three-probe (contact) and four-probe (graphene channel) resistances as a function of time measured at high bias currents of 2 and 1 mA, respectively. (b) Optical images of the CVD graphene on SiO₂/Si substrate with Co/TiO₂ tunnel contact before and after the electrical breakdown.

terminals and four-terminals measurements were performed using a Keithley current source (with currents 100, 200, 500, and 1,000 μA for spin transport measurements) and a nanovoltmeter. Cyclic four probe current-voltage measurements were carried out with a Keithley sourcemeter.

Acknowledgements

We gratefully acknowledge funding from the European Research Council (ERC) Project SPINNER, Swedish Research Council (VR Starting Grants 2016–03278, 2017–05030, as well as project grant 2021-03675), Stiftelsen Olle Engkvist Byggmästare (No. 200–0602), Energimyndigheten (No. 48698–1), Formas (No. 2019–01326), and Wenner-Gren Stiftelserna (Nos. UPD2018-0003 and UPD2019-0166).

Funding note Open Access funding provided by Uppsala University.

Electronic Supplementary Material: Supplementary material (Raman spectra of CVD graphene, low current device characterization (electrical and spin transport), 3T and 4T characterization up to high currents) is available in the online version of this article at <https://doi.org/10.1007/s12274-022-5174-9>.

Open Access This article is licensed under a Creative Commons Attribution 4.0 International License, which permits use, sharing, adaptation, distribution and reproduction in any medium or format, as long as you give appropriate credit to the original author(s) and the source, provide a link to the Creative Commons licence, and indicate if changes were made.

The images or other third party material in this article are included in the article's Creative Commons licence, unless indicated otherwise in a credit line to the material. If material is not included in the article's Creative Commons licence and your intended use is not permitted by statutory regulation or exceeds the permitted use, you will need to obtain permission directly from the copyright holder.

To view a copy of this licence, visit <http://creativecommons.org/licenses/by/4.0/>.

References

- [1] Avsar, A.; Ochoa, H.; Guinea, F.; Özyilmaz, B.; van Wees, B. J.; Vera-Marun, I. J. Colloquium: Spintronics in graphene and other two-dimensional materials. *Rev. Mod. Phys.* **2020**, *92*, 021003.
- [2] Wang, P. C.; Filippi, R. G. Electromigration threshold in copper interconnects. *Appl. Phys. Lett.* **2001**, *78*, 3598–3600.
- [3] Muñoz, R.; Gómez-Alexandre, C. Review of CVD synthesis of graphene. *Chem. Vap. Depos.* **2013**, *19*, 297–322.
- [4] Kim, K. S.; Zhao, Y.; Jang, H.; Lee, S. Y.; Kim, J. M.; Kim, K. S.; Ahn, J. H.; Kim, P.; Choi, J. Y.; Hong, B. H. Large-scale pattern growth of graphene films for stretchable transparent electrodes. *Nature* **2009**, *457*, 706–710.
- [5] Mishra, H.; Panda, J.; Maddu, R.; Sarkar, T.; Dayen, J. F.; Belotcerkotceva, D.; Kamalakar, M. V. Experimental advances in charge and spin transport in chemical vapor deposited graphene. *J. Phys. Mater.* **2021**, *4*, 042007.
- [6] Kamalakar, M. V.; Groenveld, C.; Dankert, A.; Dash, S. P. Long distance spin communication in chemical vapour deposited graphene. *Nat. Commun.* **2015**, *6*, 6766.
- [7] Gebeyehu, Z. M.; Parui, S.; Sierra, J. F.; Timmermans, M.; Esplandiu, M. J.; Brems, S.; Huyghebaert, C.; Garello, K.; Costache, M. V.; Valenzuela, S. O. Spin communication over 30 μm long channels of chemical vapor deposited graphene on SiO_2 . *2D Mater.* **2019**, *6*, 034003.
- [8] Serrano, I. G.; Panda, J.; Denoel, F.; Vallin, Ö.; Phuyal, D.; Karis, O.; Kamalakar, M. V. Two-dimensional flexible high diffusive spin circuits. *Nano Lett.* **2019**, *19*, 666–673.
- [9] Panda, J.; Ramu, M.; Karis, O.; Sarkar, T.; Kamalakar, M. V. Ultimate spin currents in commercial chemical vapor deposited graphene. *ACS Nano* **2020**, *14*, 12771–12780.
- [10] Moser, J.; Barreiro, A.; Bachtold, A. Current-induced cleaning of graphene. *Appl. Phys. Lett.* **2007**, *91*, 163513.
- [11] Murali, R.; Yang, Y. X.; Brenner, K.; Beck, T.; Meindl, J. D. Breakdown current density of graphene nanoribbons. *Appl. Phys. Lett.* **2009**, *94*, 243114.
- [12] Novoselov, K. S.; McCann, E.; Morozov, S. V.; Fal'ko, V. I.; Katsnelson, M. I.; Zeitler, U.; Jiang, D.; Schedin, F.; Geim, A. K. Unconventional quantum hall effect and Berry's phase of 2π in bilayer graphene. *Nat. Phys.* **2006**, *2*, 177–180.
- [13] Lee, K. J.; Chandrasekaran, A. P.; Kong, J. Breakdown current density of CVD-grown multilayer graphene interconnects. *IEEE Electron Device Lett.* **2011**, *32*, 557–559.
- [14] Debroy, S.; Sivasubramani, S.; Vaidya, G.; Acharyya, S. G.; Acharyya, A. Temperature and size effect on the electrical properties of monolayer graphene based interconnects for next generation MQCA based nanoelectronics. *Sci. Rep.* **2020**, *10*, 6240.
- [15] Kim, K.; Lee, Z.; Regan, W.; Kisielowski, C.; Crommie, M. F.; Zettl, A. Grain boundary mapping in polycrystalline graphene. *ACS Nano* **2011**, *5*, 2142–2146.
- [16] Fan, X.; Wagner, S.; Schädlich, P.; Speck, F.; Kataria, S.; Haraldsson, T.; Seyller, T.; Lemme, M. C.; Niklaus, F. Direct observation of grain boundaries in graphene through vapor hydrofluoric acid (VHF) exposure. *Sci. Adv.* **2018**, *4*, eaar5170.
- [17] Grosser, K. L.; Dorgan, V. E.; Estrada, D.; Wood, J. D.; Vlassiouk, I.; Eres, G.; Lyding, J. W.; King, W. P.; Pop, E. Direct observation of resistive heating at graphene wrinkles and grain boundaries. *Appl. Phys. Lett.* **2014**, *105*, 143109.
- [18] Belotcerkotceva, D.; Maciel, R. P.; Berggren, E.; Maddu, R.; Sarkar, T.; Kvashnin, Y. O.; Thonig, D.; Lindblad, A.; Eriksson, O.; Kamalakar, M. V. Insights and implications of intricate surface charge transfer and sp^3 -defects in graphene/metal oxide interfaces. *ACS Appl. Mater. Interfaces* **2022**, *14*, 36209–36216.
- [19] Yu, T. H.; Lee, E. K.; Briggs, B.; Nagabhirava, B.; Yu, B. Bilayer graphene system: Current-induced reliability limit. *IEEE Electron Device Lett.* **2010**, *31*, 1155–1157.
- [20] Banszerus, L.; Schmitz, M.; Engels, S.; Goldsche, M.; Watanabe, K.; Taniguchi, T.; Beschoten, B.; Stampfer, C. Ballistic transport exceeding 28 μm in CVD grown graphene. *Nano Lett.* **2016**, *16*, 1387–1391.
- [21] Verguts, K.; Defossez, Y.; Leonhardt, A.; De Messemaeker, J.; Schouteden, K.; Van Haesendonck, C.; Huyghebaert, C.; De Gendt, S.; Brems, S. Growth of millimeter-sized graphene single crystals on Al_2O_3 (0001)/Pt (111) template wafers using chemical vapor deposition. *ECS J. Solid State Sci. Technol.* **2018**, *7*, M195–M200.
- [22] Vera-Marun, I. J.; van den Berg, J. J.; Dejene, F. K.; van Wees, B. J. Direct electronic measurement of Peltier cooling and heating in graphene. *Nat. Commun.* **2016**, *7*, 11525.
- [23] Breitenstein, O.; Warta, W.; Langenkamp, M. *Lock-in Thermography*; Springer Berlin, Heidelberg, 2005.
- [24] Harzheim, A.; Spiece, J.; Evangelisti, C.; McCann, E.; Falko, V.; Sheng, Y. W.; Warner, J. H.; Briggs, G. A. D.; Mol, J. A.; Gehring, P. et al. Geometrically enhanced thermoelectric effects in graphene nanoconstrictions. *Nano Lett.* **2018**, *18*, 7719–7725.
- [25] Sierra, J. F.; Neumann, I.; Costache, M. V.; Valenzuela, S. O. Hot-carrier seebeck effect: Diffusion and remote detection of hot carriers in graphene. *Nano Lett.* **2015**, *15*, 4000–4005.
- [26] Bakker, F. L.; Slachter, A.; Adam, J. P.; van Wees, B. J. Interplay of peltier and seebeck effects in nanoscale nonlocal spin valves. *Phys. Rev. Lett.* **2010**, *105*, 136601.
- [27] Sierra, J. F.; Neumann, I.; Cuppens, J.; Raes, B.; Costache, M. V.; Valenzuela, S. O. Thermoelectric spin voltage in graphene. *Nat. Nanotechnol.* **2018**, *13*, 107–111.
- [28] Parkin, S. S. P.; Kaiser, C.; Panchula, A.; Rice, P. M.; Hughes, B.; Samant, M.; Yang, S. H. Giant tunnelling magnetoresistance at room



- temperature with MgO (100) tunnel barriers. *Nat. Mater.* **2004**, *3*, 862–867.
- [29] Zhang, S.; Levy, P. M.; Marley, A. C.; Parkin, S. S. P. Quenching of magnetoresistance by hot electrons in magnetic tunnel junctions. *Phys. Rev. Lett.* **1997**, *79*, 3744–3747.
- [30] Levy, P. M.; Fert, A. Spin transfer in magnetic tunnel junctions with hot electrons. *Phys. Rev. Lett.* **2006**, *97*, 097205.
- [31] Fert, A.; Jaffrèse, H. J. Conditions for efficient spin injection from a ferromagnetic metal into a semiconductor. *Phys. Rev. B* **2001**, *64*, 184420.
- [32] Durkan, C.; Xiao, Z. C. On the failure of graphene devices by joule heating under current stressing conditions. *Appl. Phys. Lett.* **2015**, *107*, 243505.
- [33] Neumann, I.; Costache, M. V.; Bridoux, G.; Sierra, J. F.; Valenzuela, S. O. Enhanced spin accumulation at room temperature in graphene spin valves with amorphous carbon interfacial layers. *Appl. Phys. Lett.* **2013**, *103*, 112401.
- [34] Kamalakar, M. V.; Dankert, A.; Bergsten, J.; Ive, T.; Dash, S. P. Enhanced tunnel spin injection into graphene using chemical vapor deposited hexagonal boron nitride. *Sci. Rep.* **2014**, *4*, 6146.
- [35] Kamalakar, M. V.; Dankert, A.; Kelly, P. J.; Dash, S. P. Inversion of spin signal and spin filtering in ferromagnet|hexagonal boron nitride|graphene van der Waals heterostructures. *Sci. Rep.* **2016**, *6*, 21168.
- [36] Gurram, M.; Omar, S.; van Wees, B. J. Electrical spin injection, transport, and detection in graphene-hexagonal boron nitride van der Waals heterostructures: Progress and perspectives. *2D Mater.* **2018**, *5*, 032004.
- [37] Friedman, A. L.; van 't Erve, O. M. J.; Li, C. H.; Robinson, J. T.; Jonker, B. T. Homoepitaxial tunnel barriers with functionalized graphene-on-graphene for charge and spin transport. *Nat. Commun.* **2014**, *5*, 3161.
- [38] Dayen, J. F.; Ray, S. J.; Karis, O.; Vera-Marun, I. J.; Kamalakar, M. V. Two-dimensional van der Waals spinterfaces and magnetic-interfaces. *Appl. Phys. Rev.* **2020**, *7*, 011303.